Microfluid Nanofluid (2011) 11:129–136
DOI 10.1007/s10404-011-0779-4

RESEARCH PAPER

Persistence of turbulent flow in microchannels at very low Reynolds numbers

Peter Lammers · Jovan Jovanović · Antonio Delgado

Received: 25 August 2010 / Accepted: 11 February 2011 / Published online: 25 February 2011

Abstract A fully resolved numerical simulation of a turbulent microchannel flow, with uniformly spaced two-dimensional obstruction elements mounted at the wall and normal to the flow direction, was carried out at a very low Reynolds number of $Re \simeq 970$ based on the centerline velocity and the microchannel height. Employing the lattice Boltzmann numerical technique, all energetic scales of turbulence were resolved with about 19×10^6 grid points ($1261 \times 129 \times 128$ in the x_1, x_2, and x_3 directions). The simulated results confirm the self-maintenance of turbulence at such a low Reynolds number. Turbulence persisted over more than 1,000 turnover times, which was sufficiently long to prove its self-maintenance. These findings support the conjecture that turbulence developing in microchannels having rough walls can not only be initiated but also maintained at very low Reynolds numbers.

1 Introduction

Microchannels and microtubes are nowadays playing important roles in microfluidics devices known as MEMS (Micro-Electro-Mechanical Systems). Owing to technological limitations in manufacturing, the surface roughness in such devices consisting of channels or tubes is comparable to their cross-section dimensions. An interesting aspect of fluid mechanics through microfluidic devices is related to the appearance and self-maintenence of turbulence at very low Reynolds numbers.

The major goal of this study was to investigate numerically circumstances which lead to the production and self-maintenance of turbulence at very low Reynolds numbers. Experiments made in small glass and brass capillary pipes revealed that turbulence can be maintained at very low Reynolds numbers if the wall boundaries are rough (Ruckes 1907). New experimental results (Hao et al. 2006) obtained by employing Micro Particle Image Velocimetry (μPIV) also suggest that the flow becomes fully turbulent in the rough microchannels at very low Reynolds numbers.

It was decided to initiate a numerical program, using a state-of-the-art lattice Boltzmann numerical technique, in order to realize virtually turbulence at very low Reynolds numbers. This was achieved by placing regularly spaced, two-dimensional obstruction elements at the wall in a such way that they were arranged normal to the flow direction in a microchannel. Such a configuration forces turbulence, in the near-wall region, to restructure in order to promote its production and insure its self-maintenance at very low Reynolds number.

2 Computational flow domain

The computed flow arrangement and the coordinate system employed are presented in Fig. 1. For wall-bounded flows, the characteristic scales are defined using parameters that are defined at the wall boundaries, such as the fluid density ρ, kinematic viscosity of the fluid ν and the wall shear

P. Lammers
CD-adapco, Nordost Park 3-5, 90411 Nuremberg, Germany
e-mail: peter.lammers@de.cd-adapco.com

J. Jovanović · A. Delgado
Institute of Fluid Mechanics, Friedrich-Alexander University Erlangen-Nuremberg, Cauerstrasse 4, 91058 Erlangen, Germany

A. Delgado
e-mail: antonio.delgado@lstm.uni-erlangen.de

J. Jovanović (✉)
Center of Smart Interfaces, Technische Universität Darmstadt, Petersenstrasse 32, 64287 Darmstadt, Germany
e-mail: jovan.jovanovic@lstm.uni-erlangen.de

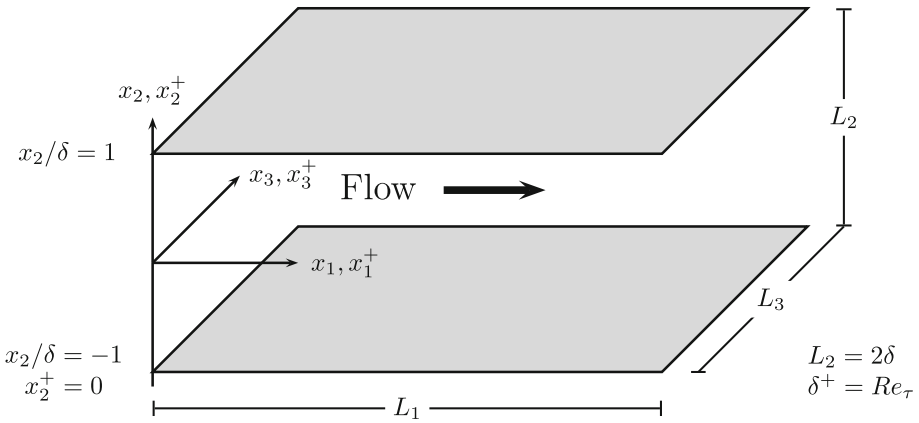

Fig. 1 Computational flow domain of a microchannel and coordinate system

stress τ_w. From these parameters emerges the velocity scale u_τ as follows:

$$u_\tau = \sqrt{\frac{\tau_w}{\rho}}, \tag{1}$$

which is related to the mean streamwise pressure-gradient $\partial\overline{P}/\partial x_1$ through the momentum equations by

$$u_\tau = \sqrt{\frac{\delta}{\rho}\frac{\partial\overline{P}}{\partial x_1}}, \tag{2}$$

where δ is the microchannel half-width. In terms of the parameters mentioned above, the length scale emerges as $l_\tau = \nu/u_\tau$. Following usual practice, all variables are normalized using these inner scales and this is identified in the text by the superscript +, e.g., $x^+ = xu_\tau/\nu$.

There are two options for performing numerical simulations of a turbulent microchannel flow: either to fix the flow rate through the microchannel or to prescribe the axial pressure-gradient and therefore u_τ. For these simulations, the authors chose the latter approach and thereby the Reynolds number Re_τ, based on $\tilde{u}_\tau$ calculated from (2) and the microchannel half-width, was fixed, for the flow simulation described below, at the value

$$Re_\tau = \frac{\delta\tilde{u}_\tau}{\nu} = \delta^+ \simeq 60. \tag{3}$$

In order to insure the persistence of turbulence at very low Reynolds numbers, 15 regularly spaced two-dimensional obstruction elements were placed at the microchannel walls and normal to the flow direction. A schematic arrangement of the simulated configuration is presented in Fig. 2.

The obstruction elements were uniformly separated by a distance $d^+ \simeq 90$ and arranged symmetrically, $D^+ = 0$, on the top and bottom sides of the microchannel. The non-dimensional height and the width of the obstruction elements were $h^+ \simeq 16$ and $w^+ \simeq 0.9375$, respectively. For these dimensions, the blockage ratio was 30% (which is defined as the ratio of the cross-sectional area occupied by the obstruction element to the cross-sectional area of the empty microchannel).

For the configuration shown in Fig. 2, the flow is homogeneous in the spanwise direction and quasi-homogeneous in the flow direction if the number of obstruction elements N is sufficiently large. Assuming that $N = 15$ satisfies the latter requirement, periodic boundary conditions were used in the x_1 and x_3 directions. Employing an equidistant cartesian grid with $1261 \times 129 \times 128$ points in the x_1, x_2 and x_3 directions, the non-dimensional grid spacing was $\Delta x_i^+ = 0.9375$.

The adequacy of the space resolution of a simulation performed for a configuration with obstruction elements is presented in Fig. 3. The results reveal that the grid resolution was sufficiently fine to resolve all essential turbulence scales. The estimated value of the Kolmogorov length scale $\eta = (\nu^3/\varepsilon_h)^{1/4}$ obtained from the average

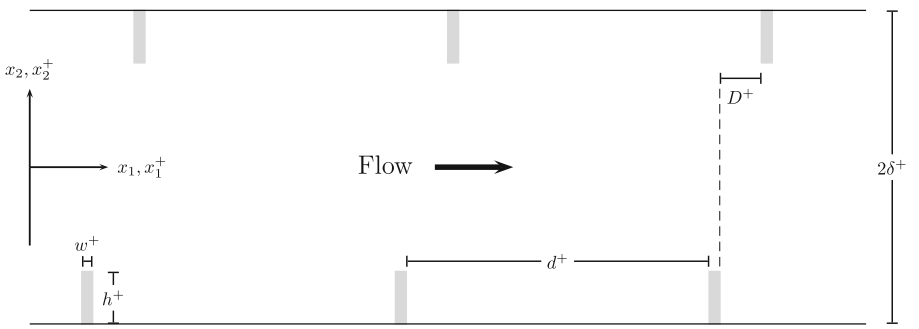

Fig. 2 Arrangement of the obstruction elements mounted at the walls in a microchannel. The elements are extended in the spanwise direction x_3 (see Fig. 1). Only a small part of the simulated domain is shown

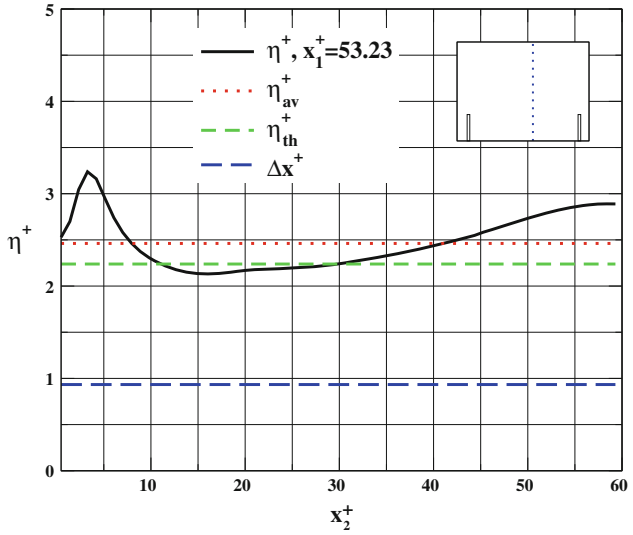

Fig. 3 Distribution of the grid spacing (Δx_i^+) and the local (η^+) and average ($\eta^+_{\rm av}$) Kolmogorov length scale for the microchannel configuration shown in Fig. 2

dissipation rate across the channel per unit mass of the working fluid was $\eta^+_{\rm th} \simeq 2.25$.

3 Numerical technique

The choice of the numerical technique was primarily motivated by the requirement for an efficient algorithm with small computing costs per grid point and time step. Owing to the complex flow configuration, the lattice Boltzmann method (LBM) was a straightforward and attractive choice and will be briefly described (see, Lammers 2004).

The LBM was developed during the last decade as an alternative approach to classical methods of numerical fluid dynamics. The method utilizes the fact that information on the velocity **U** and the pressure p of a viscous fluid can be deduced by solving a kinetic equation for a one-particle distribution function f instead of Navier-Stokes equations directly. The function $\tilde{f} = \tilde{f}(\xi, \mathbf{r}, t)$ depends on the molecular velocity ξ, the position in space $\mathbf{r}$ and the time $\tilde{t}$. The flow quantities are obtained from the moments of the distribution function.

A very popular and widely employed kinetic model is described by the Boltzmann equation together with the so-called Bhatnagar-Gross-Krook (BGK) ansatz (Bhatnagar 1954) for the collision operator

$$(\partial_{\tilde{t}} + \xi \nabla_{\mathbf{r}} + \mathcal{F} \nabla_{\xi}) \tilde{f}(\xi, \mathbf{r}, \tilde{t}) = -\frac{\tilde{f}(\xi, \mathbf{r}, \tilde{t}) - \tilde{f}^{eq}(\xi, \mathbf{r}, \tilde{t})}{\lambda}, \tag{4}$$

where $\mathcal{F}$ is the external force. The function $\tilde{f}^{eq}$ corresponds to the equilibrium (Maxwell-Boltzmann) distribution and λ is a relaxation time. This equation is discretized in time and space. In addition, a finite set of velocities $\mathbf{c}_i$ for ξ has to be defined. As a result of discretization, the following non-dimensional equation is obtained:

$$f_i(\mathbf{x} + \mathbf{c}_i, t+1) - f_i(\mathbf{x}, t) = -\omega(f_i(\mathbf{x}, t) - f_i^{eq}(\rho, \mathbf{U} + \tfrac{\mathcal{E}}{2\rho}, \mathbf{x}, t)) + 3t_p \tfrac{2-\omega}{2} \mathbf{c}_i \mathcal{E}, \tag{5}$$

where f_i is the distribution function of the velocity $\mathbf{c}_i$. A detailed derivation of how the lattice Boltzmann equation recovers the Navier-Stokes equation can be found in (Hou et al. 1995) and especially for Eq. 5 in (Buick and Greated 2000).

Equation 5 appears to be a first-order scheme but is in fact second order in time (He and Luo 1997). Without loss of generality the authors may choose $\delta t = 1$ for the time step and $\rho = 1$ for the density. The force density $\mathcal{E}$ is given by the pressure gradient according to $\mathcal{E} = \nabla p$, whereby $\mathcal{E}_1$ is the only remaining component in this case. The macroscopic behavior of Eq. 5 is obtained by a Chapman-Enskog procedure (Chapman and Cowling 1999) together with a Taylor expansion of the Maxwell-Boltzmann equilibrium distribution for small velocity (small Mach number). For this equilibrium distribution

$$f_i^{eq} = t_p \rho \left\{ 1 + \frac{c_{i_\alpha} U_\alpha}{c_s^2} + \frac{U_\alpha U_\beta}{2c_s^2} \left(\frac{c_{i_\alpha} c_{i_\beta}}{c_s^2} - \delta_{\alpha\beta} \right) \right\} \tag{6}$$

it can be shown that the Mach number must be $|u/c_s| \ll 1$ in order to satisfy the incompressible Navier-Stokes equations. The parameters t_p and $p = \|\mathbf{c}_i\|^2$ depend on the discretization of the molecular velocity space. Various model formulations can be found in (Qian et al. 1992). For this simulation a three-dimensional model with 19 velocities $\mathbf{c}_i$, $i = 0, \ldots, 18$ (D3Q19) was employed. The D3Q19 model has the parameters $t_0 = 1/3$, $t_1 = 1/18$ and $t_2 = 1/36$. A sketch of $\mathbf{c}_i$ is given in Fig. 4.

The implementation of the LBM is validated against the pseudo-spectral simulation (Kim et al. 1987; Moser et al. 1999) for plane channel flow at $Re_\tau \approx 180$. Figure 5

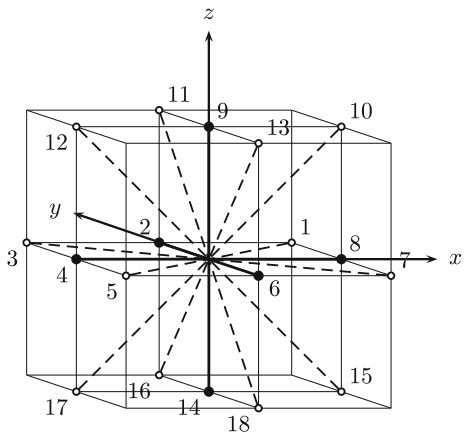

Fig. 4 Employed lattice geometry and the velocity vectors $\mathbf{c}_i$ for the three-dimensional 19-velocity D3Q19 model

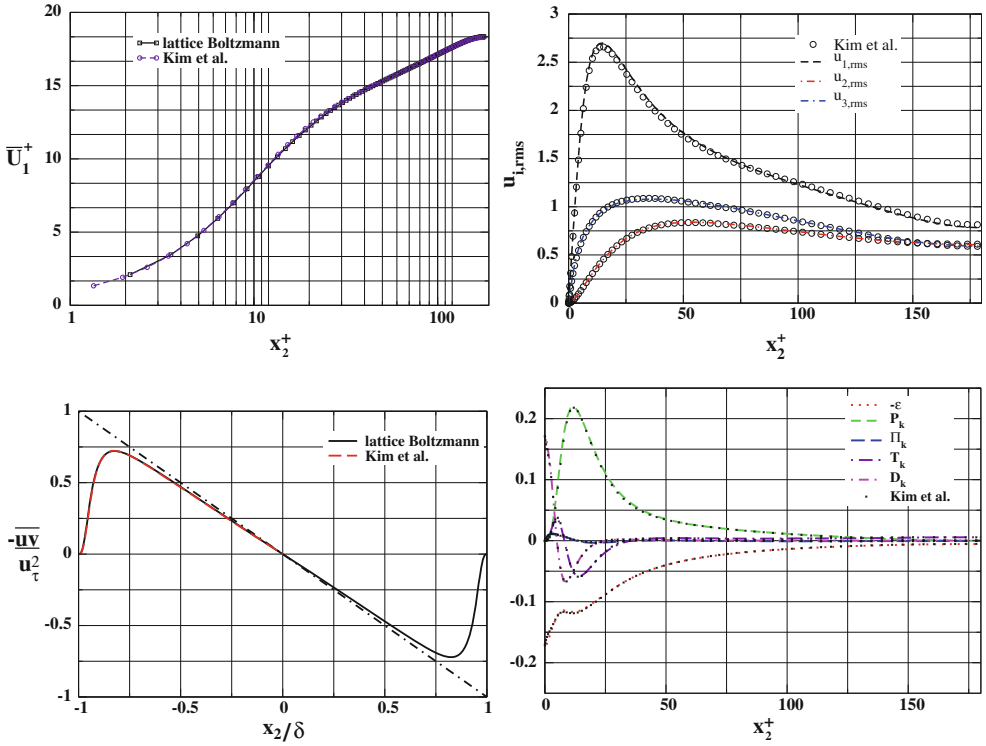

Fig. 5 Comparison of a lattice Boltzmann and a pseudo-spectral simulation (Kim et al. 1987; Moser et al. 1999) for a plane channel flow at $Re_\tau \approx 180$. Non-dimensionalized profiles of mean velocity, root-mean-square velocity fluctuations, turbulent shear-stress $\overline{u_1 u_2}$ and the balance of the k equation all scaled on the inner variables

demonstrates that profiles of the mean velocity, root-mean-square velocity fluctuations, turbulent shear-stress $\overline{u_1 u_2}$ and the balance of the energy ($k = 1/2\overline{u_k u_k}$) equation agree closely with the results of the study mentioned above. It is worth noting that the results displayed in Fig. 5 were obtained with a grid size of $4096 \times 257 \times 256$, resulting in a resolution $\Delta x_i^+ = 1.4$. This resolution is nearly twice as coarse as that for the simulation performed for a channel configuration with the obstruction elements.

4 Simulation results

Starting from the initial field, the governing equations were integrated until the simulated flow field reached a statistically steady state. This state was identified by sampling running averages of the turbulence statistics very close to the wall and at the channel centerline. Figure 6 shows that the relative turbulence intensity converges to about 40% close to the wall and 10% at the channel centerline, which is consistent with the experimental data measured in a fully developed turbulent channel flow at low Reynolds numbers (Fischer et al. 2001). When the statistically stationary state had been reached, the equations were additionally integrated in order to prove self-maintenance of turbulence over a sufficiently long interval of time and to increase the statistical sample for the evaluation of various correlations of interest. Calculations

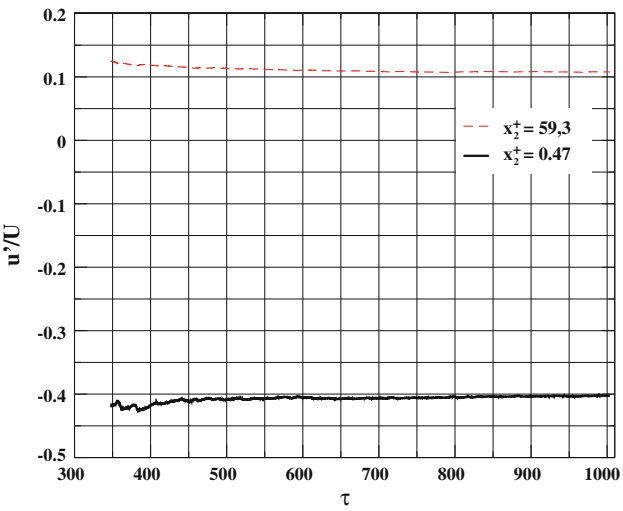

Fig. 6 Relative turbulence intensity $u_1'/\overline{U}_1$ at two monitoring locations close to the wall (*bottom* $-u_1'/\overline{U}_1$) and at the channel centerline (*top*) as a function of normalized time $\tau = t/(\delta/u_\tau)$ of integration. These results confirm the persistence and self-maintenance of turbulence over more than 1,000 turnover times (δ/u_τ)

of the plane channel flow with smooth walls starting from identical initial and boundary conditions yielded a laminar flow field after only a few integration time steps.

After the simulations had reached a statistically stationary state, the mean flow quantities were determined by

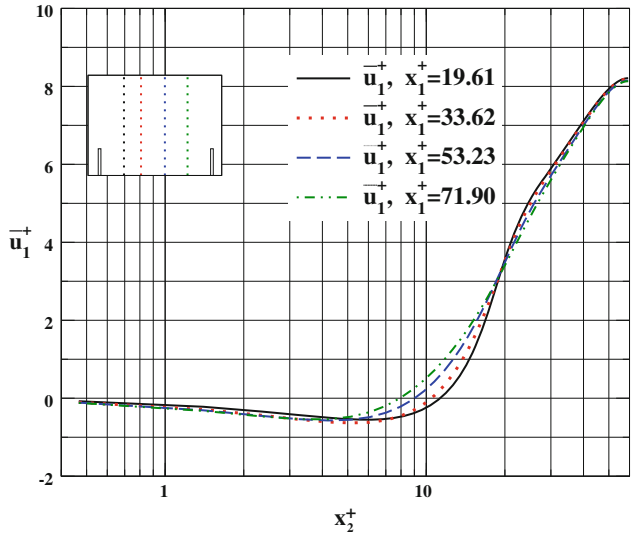

Fig. 7 Normalized mean velocity profiles in the flow direction

averaging instantaneous flow realizations over time and also over the vertical planes along the gap between two neighboring obstruction elements. For large numbers of symmetrically arranged and regularly spaced obstruction elements, such averaging is permitted since the mean flow field is expected to be symmetrical and quasi-periodic in the streamwise direction. This specific type of time and space averaging allowed a considerable increase in the sample for the determination of turbulence statistics.

The profiles of the mean velocity in the flow direction for four cross-sections between the obstruction elements are shown in Fig. 7. These data are non-dimensionalized by the wall friction velocity $\overline{U}_1^+ = \overline{U}_1/\tilde{u}_\tau$ calculated from the pressure gradient along the microchannel using (2) and plotted versus the normalized distance from the wall $x_2^+ = x_2\tilde{u}_\tau/\nu$. The quasi-self-similarity of these profiles in inner scaling implies that the flow is dominated entirely by the condition at the solid surface. The flow in the near-wall region is very weak and shows clear signs of reversal. The reversed flow occupies the entire gap between the two obstruction elements. The data in Fig. 7 show that the simulated results correspond to a Reynolds number of

$$Re_c = \frac{2\delta\,\overline{U}_c}{\nu} \approx 970, \tag{7}$$

based on the full microchannel height (2δ) and the mean centerline velocity ($\overline{U}_c$).

The profiles of all three turbulence intensity components $u_i' = \sqrt{\overline{u_i^2}}$, $i = 1, 2, 3$, normalized with $\tilde{u}_\tau$ are presented in Fig. 8. The data displayed show that the fluctuating velocity components are reasonably correlated with $\tilde{u}_\tau$ across the

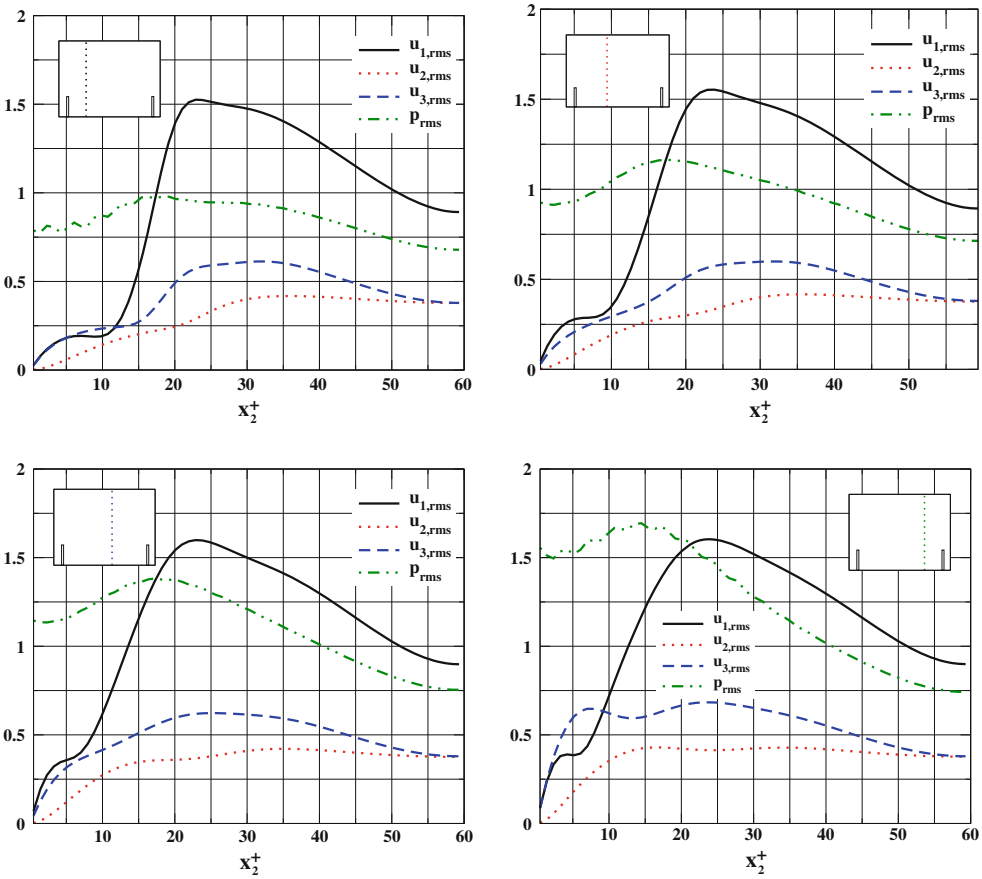

Fig. 8 Non-dimensionalized root-mean-square velocity fluctuations versus the normalized distance from the wall: (*top left*) $x_1^+ = 19.61$; (*top right*) $x_1^+ = 33.62$; (*bottom left*) $x_1^+ = 53.23$; (*bottom right*) $x_1^+ = 71.90$

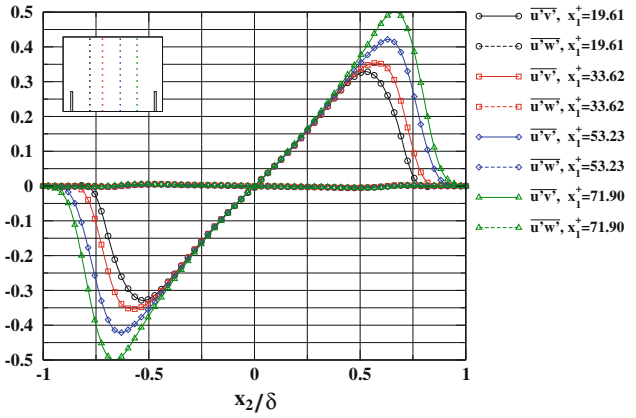

Fig. 9 Turbulent shear stresses $\overline{u_1u_2}$ and $\overline{u_1u_3}$ non-dimensionalized with $\tilde{u}_\tau$ versus the normalized distance from the wall x_2/δ

entire flow field. The general shape of these profiles differs considerably from those of the smooth channel shown in Fig. 5. The maximum of turbulent intensity is shifted away from the near-wall region and the intensities of normal and spanwise velocity components are lower than for turbulence developing along the smooth boundaries.

The turbulent shear-stress profiles normalized in inner scaling are shown in Fig. 9. Owing to the broken homogeneity in the streamwise direction because of the presence of the obstruction elements, apart from $\overline{u_1u_2}$, additional shear stress $\overline{u_1u_3}$ exists which is, however, very small. The computed profiles of $\overline{u_1u_2}$ reveal that it is negligible across the entire region separated between the obstruction elements. In the region above the obstruction elements $\overline{u_1u_2}$ shows a linear rise up to the microchannel centerline. This behavior of $\overline{u_1u_2}$ is similar to the shear stress development in a channel flow with smooth walls, shown in Fig. 5, with the difference, however, that the overall level is much lower.

Figure 10 shows traces of joint variations of invariants $\mathrm{II_a} = \mathrm{a_{ij}a_{ji}}$ and $\mathrm{III_a} = \mathrm{a_{ij}a_{jk}a_{ki}}$ of the anisotropy tensor $a_{ij} = \overline{u_iu_j}/q^2 - 1/3\delta_{ij}$ across the anisotropy-invariant map. This figure indicates that the obstruction elements force the anisotropy very close to the wall to decrease compared with the flow with smooth walls. As a consequence, the invariants, which lie along the two-component state, shift toward the left corner point of the anisotropy map, which corresponds to two-component isotropic turbulence. Examination of the simulated data presented in Fig. 8 reveals that the obstruction elements significantly suppress streamwise velocity fluctuations near the wall. Owing to the blockage effect of the obstruction elements, the streamwise and the spanwise velocity fluctuations grow at approximately the same rate close to the wall. Such behavior of the velocity fluctuations prevents large anisotropy from developing in the near-wall region, which is the essential feature of turbulence developing along smooth boundaries at low Reynolds numbers (Fig. 10, left). Hence, the simulated results suggest that the chief mechanism associated with self-maintenance of turbulence at very low Reynolds numbers is related to a reduction of anisotropy in the velocity fluctuations close to the solid boundary.

The budget of the turbulent kinetic energy $k = 1/2\overline{u_su_s}$:

$$\underbrace{\frac{\partial k}{\partial t} + \overline{U}_k\frac{\partial k}{\partial x_k}}_{Dk/Dt} = \underbrace{-\overline{u_iu_k}\frac{\partial \overline{U}_i}{\partial x_k}}_{P_k} \underbrace{-\nu\overline{\frac{\partial u_i}{\partial x_k}\frac{\partial u_i}{\partial x_k}}}_{\varepsilon} \underbrace{-\frac{1}{2}\frac{\partial \overline{u_su_su_k}}{\partial x_k}}_{T_k} \underbrace{-\frac{1}{\rho}\frac{\partial \overline{pu_k}}{\partial x_k}}_{\Pi_k} + \underbrace{\nu\frac{\partial^2 k}{\partial x_k\partial x_k}}_{D_k}, \quad (8)$$

is shown in Fig. 11. All terms involved in the balance of the k equation, convection Dk/Dt, production P_k, turbulent transport T_k, pressure transport Π_k, viscous dissipation ε and the viscous diffusion D_k, are normalized with inner variables. The computed data show that the production and the viscous

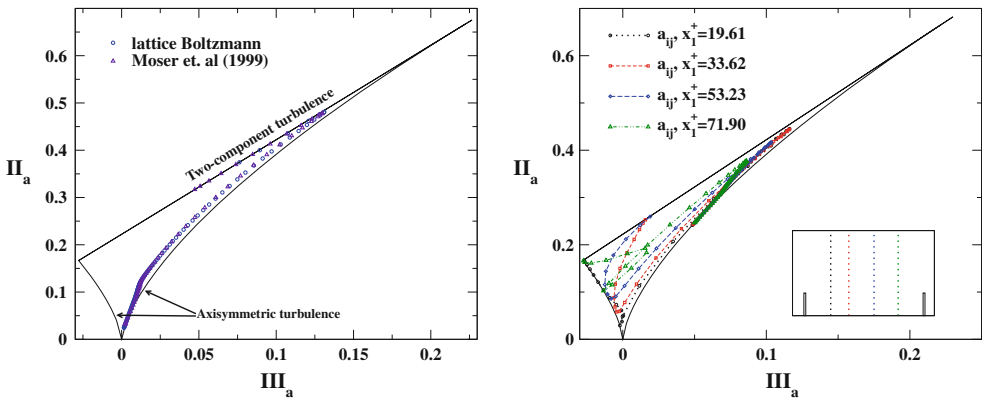

Fig. 10 Anisotropy-invariant mapping of low Reynolds number turbulence in wall-bounded flows: *left* turbulence developing in plane channel flow with smooth walls; *right* turbulence developing in microchannel with obstruction elements mounted at the walls and perpendicular to the flow direction

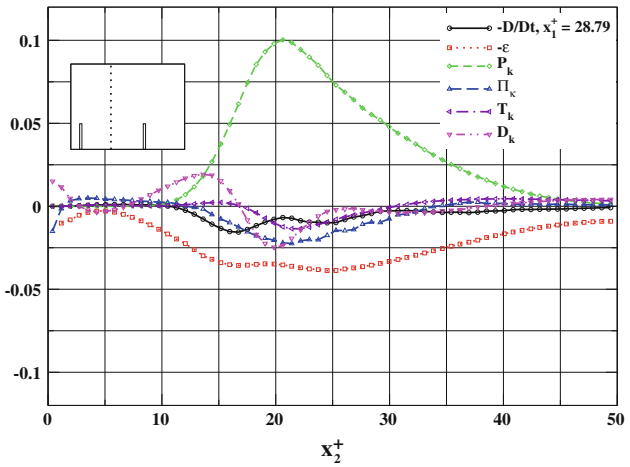

Fig. 11 Terms contributing to the balance of the energy k equation normalized by $\tilde{u}_\tau{}^4/\nu^2$

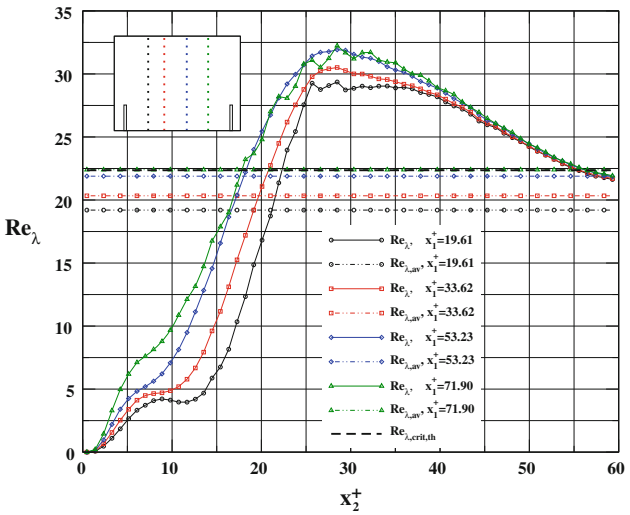

Fig. 12 Distributions of local and volume-averaged turbulent Reynolds number $R_\lambda = q\lambda/\nu$ in the region between the obstruction elements and comparisons with the transition criterion $(R_\lambda)_{\text{crit}} \approx 10\sqrt{5}$

dissipation processes are dominant in the balance of k. These two processes are, however, out of equilibrium across the entire flow domain. In the region between the obstruction elements, turbulent dissipation and the viscous diffusion dominate and are balanced by production, convection, turbulent, and pressure transport. In the outer flow, above the obstruction elements, the production process is dominant in the budget of the k equation and is balanced partially by the dissipation and by other processes of transport nature.

The numerical results presented in this study provide an opportunity for validation of the theoretical consideration of the transition process derived by the authors (Jovanović and Pashtrapanska 2004) which leads to the criterion for the estimation of the transition onset and breakdown to turbulence in wall-bounded flows. Figure 12 shows local (R_λ) and volume-averaged ($\overline{R_\lambda}$) data for the turbulent Reynolds number $R_\lambda = \lambda\, q/\nu$ based on Taylor's microscale $\lambda = (5\nu q^2/\varepsilon_h)^{1/2}$, where ε_h is the homogeneous part of the turbulent dissipation rate:

$$\varepsilon = \nu\overline{\frac{\partial u_i}{\partial x_k}\frac{\partial u_i}{\partial x_k}} = \frac{1}{4}\nu\frac{\partial^2 q^2}{\partial x_k \partial x_k} + \varepsilon_h. \tag{9}$$

Figure 12 also shows comparisons with the transition criterion:

$$(\overline{R_\lambda})_{\text{crit}} \approx 10\sqrt{5}, \tag{10}$$

derived in (Jovanović and Pashtrapanska 2004), which suggests the permissible magnitudes for the intensity (q) and the length scale (λ) of the disturbances which guarantee maintenence of the laminar flow regime if $\overline{R_\lambda} < (\overline{R_\lambda})_{\text{crit}}$ or the appearance and self-maintenance of turbulence if $\overline{R_\lambda} > (\overline{R_\lambda})_{\text{crit}}$. The data for R_λ averaged over the microchannel cross-section lie very close to the criterion mentioned above, which indicates that the flow just reached the critical conditions in the region $70 < x_1^+ < 90$.

Further simulation results including the budgets of all stress components and of the dissipation rate equation at different Reynolds numbers can be found in (Lammers 2004). These results permitted the advanced statistical analysis of low Reynolds number turbulence to be presented in the functional space, which emphasize the anisotropic nature of turbulence centered around the critical flow conditions leading either to instability and breakdown to fully developed turbulence or to flow relaminarization and reverse transition to a stable laminar state.

5 Conclusions and final remarks

A direct numerical simulation was performed of a microchannel flow, with the two-dimensional obstruction elements mounted at the walls and placed perpendicular to the flow. Using the lattice Boltzmann numerical method, all scales were resolved in the computational domain with $1261 \times 129 \times 129$ grid points. The numerical results confirm the persistence of turbulence at a Reynolds number of $Re \simeq 970$, based on the centerline velocity and full microchannel width. This study supports early experimental observations (Ruckes 1907) which indicated that an increase in the pressure drop in brass capillary pipes was caused by surface roughness which induced the appearance of turbulence at much lower Reynolds numbers than in those made of glass material. Recent experimental results (Hao et al. 2006) also confirm the persistence of turbulence in microchannels with rough walls at very low Reynolds numbers.

The computed turbulence levels at the microchannel centerline and in close proximity to the wall were found to be in agreement with typical values for a fully developed turbulent channel flow. The collapse of the mean velocity profiles and the self-similarity of turbulence statistics when scaled on inner variables demonstrate that the simulated flow is controlled entirely by conditions at the wall. Examination of the energy balance suggests that the flow is out of equilibrium and that the production of energy is larger than the viscous dissipation.

Acknowledgments The work presented was funded in part by Deusche Forschungsgemeinchaft through grant Jo 240/5-2. The second author gratefully acknowledge this support.

References

Bhatnagar P, Gross EP, Krook MK (1954) A model for collision processes in gases. I. Small amplitude processes in charged and neutral one-component systems. Phys Rev 94:511–525

Buick J, Greated C (2000) Gravity in lattice Boltzmann model. Phys Rev E 61:5307–5320

Chapman S, Cowling TG (1999) The Mathematical Theory of Non-Uniform Gases. Cambridge University Press, Cambridge

Fischer M, Jovanović J, Durst F (2001) Reynolds number effects in the near–wall region of turbulent channel flows. Phys Fluids 13:1755–1767

Hao PF, Yao ZH, He F, Zhu KQ (2006) Experimental investigation of water flow in smooth and rough silicon microchannels. J Micromech Microeng 16:1397–1402

He X, Luo LS (1997) Theory of the lattice Boltzmann method: from the Boltzmann equation to the lattice Boltzmann equation. Phys Rev E 56:6811–6817

Hou S, Zou Q, Chen S, Doolen G, Cogley AC (1995) Simulation of cavity flow by the lattice Boltzmann method. J Comput Phys 118:329–347

Jovanović J, Pashtrapanska M (2004) On the criterion for the determination transition onset and breakdown to turbulence in wall-bounded flows. J Fluids Eng 126:626–633

Kim J, Moin P, Moser R (1987) Turbulence statistics in fully developed channel flow at low Reynolds number. J Fluid Mech 177:133–166

Lammers P (2004) Direkte numerische Simulationen wandgebundener Strömungen kleiner Reynoldszahlen mit dem lattice Boltzmann Verfahren. Ph.D. thesis, University of Erlangen-Nuremberg

Moser RD, Kim J, Mansour NN (1999) Direct numerical simulation of turbulent channel flow up to $Re_\tau = 590$. Phys Fluids 11: 943–945

Qian YH, d'Humières D, Lallemand P (1992) Lattice BGK models for Navier-Stokes equation. Europhys Lett 17:479–484

Ruckes W (1907) Untersuchungen über den Ausfluß komprimierter Luft aus Kapillaren und die dabei auftretenden Turbulenzerscheinungen. Dissertation, Kgl. Bayr. Julius-Maximilians-Universität Würzburg